EXTENDED PDF FORMAT
SPONSORED BY
usb
www.usbweb.com

Science
AAAS

Smoke Invigoration Versus Inhibition of Clouds over the Amazon

Ilan Koren, *et al.*

Science **321**, 946 (2008);
DOI: 10.1126/science.1159185

The following resources related to this article are available online at www.sciencemag.org (this information is current as of August 15, 2008):

Updated information and services, including high-resolution figures, can be found in the online version of this article at:
http://www.sciencemag.org/cgi/content/full/321/5891/946

Supporting Online Material can be found at:
http://www.sciencemag.org/cgi/content/full/321/5891/946/DC1

This article **cites 23 articles**, 6 of which can be accessed for free:
http://www.sciencemag.org/cgi/content/full/321/5891/946#otherarticles

This article appears in the following **subject collections**:
Atmospheric Science
http://www.sciencemag.org/cgi/collection/atmos

Information about obtaining **reprints** of this article or about obtaining **permission to reproduce this article** in whole or in part can be found at:
http://www.sciencemag.org/about/permissions.dtl

Science (print ISSN 0036-8075; online ISSN 1095-9203) is published weekly, except the last week in December, by the American Association for the Advancement of Science, 1200 New York Avenue NW, Washington, DC 20005. Copyright 2008 by the American Association for the Advancement of Science; all rights reserved. The title *Science* is a registered trademark of AAAS.

Table 1. Atomic positions and occupations from GIXRD analysis. Au1 to Au6 are the Au atoms in the first Au surface layer, a1 and a2 are the Au adatoms, and m1 and m2 are the S atoms.

	Occupancy	x/a	y/b	z/c
	(±0.05)		(±0.008)	
Au1	0	—	—	—
Au2	1	−0.011	0.624	−0.045
Au3	1	−0.010	0.283	−0.025
Au4	0.6 (±0.1)	0.493	0.985	−0.022
Au5	1	0.527	0.697	+0.025
Au6	1	0.530	0.351	+0.033
a1	0.6 (±0.1)	0.678	0.610	0.294
a2	0.6 (±0.1)		a1 − b/2	
m1	—	0.113	0.193	0.265
m2	—	0.523	0.396	0.365

As a consequence of these findings, studies regarding the formation, growth, diffusion, and mechanical properties of these films may need to be revisited in order to properly account for the influence of Au-S interactions and the presence of the RS-Au-SR structural motifs. From a theoretical perspective, this gives paramount importance to the development of empirical potential models that include not only molecule-molecule interactions but explicitly the Au-SR interactions, which are often neglected. In addition, our findings indicate that the adatom structures will alter the local density of states at the Fermi energy (*18*) and will affect the interpretation of electronic and magnetic properties of these materials.

References and Notes

1. A. Ulman, *Chem. Rev.* **96**, 1533 (1996).
2. F. Schreiber, *Prog. Surf. Sci.* **65**, 151 (2000).
3. J. C. Love *et al.*, *Chem. Rev.* **105**, 1103 (2005).
4. P. Maksymovych *et al.*, *Phys. Rev. Lett.* **97**, 146103 (2006).
5. R. Mazzarello *et al.*, *Phys. Rev. Lett.* **98**, 016102 (2007).
6. H. Hakkinen *et al.*, *J. Phys. Chem. B* **110**, 9927 (2006).
7. M. Yu *et al.*, *Phys. Rev. Lett.* **97**, 166102 (2006).
8. A. Nagoya *et al.*, *J. Phys. Cond. Matter* **19**, 365245 (2007).
9. H. Grönbeck *et al.*, *J. Phys. Chem. B* **111**, 3325 (2007).
10. P. D. Jadzinsky *et al.*, *Science* **318**, 430 (2007).
11. R. L. Whetten, R. C. Price, *Science* **318**, 407 (2007).
12. The conventionally termed $c(4{\times}2)$ corresponds to a $c(2\sqrt{3}\times 4\sqrt{3})$, whose primitive cell is $(2\sqrt{3}\times 3)$.
13. R. G. Nuzzo *et al.*, *J. Chem. Phys.* **93**, 767 (1990).
14. N. Camillone *et al.*, *J. Chem. Phys.* **98**, 3503 (1993).
15. P. Fenter, A. Eberhardt, P. Eisenberger, *Science* **266**, 1216 (1994).
16. D. Anselmetti *et al.*, *Europhys. Lett.* **27**, 365 (1994).
17. X. Torrelles *et al.*, *J. Phys. Chem. B* **110**, 5586 (2006).
18. C. Vericat *et al.*, *J. Phys. Cond. Matter* **18**, R867 (2006).
19. X. Torrelles *et al.*, *Langmuir* **20**, 9396 (2004).
20. M. C. Gerstenberg *et al.*, *Phys. Rev. B* **61**, 7678 (2000).
21. M. Prato *et al.*, *J. Phys. Chem. C* **112**, 3899 (2008).
22. J. G. Wang *et al.*, *J. Phys. Chem. C* **111**, 12149 (2007).
23. D. J. Lavrich *et al.*, *J. Phys. Chem. B* **102**, 3456 (1998).
24. M. C. Vargas *et al.*, *J. Phys. Chem. B* **105**, 9509 (2001).
25. G. E. Poirier, *Langmuir* **15**, 1167 (1999).
26. A. Riposan *et al.*, *J. Phys. Chem. B* **110**, 23926 (2006).
27. In our structural determination, the distance of the Au adatoms from a Au(111) crystal plane is an integer multiple of the Au lattice constant, consistent with the Au coherent fraction of the x-ray standing wave measured in (*29*).
28. J. Ulrich *et al.*, *J. Phys. Chem. B* **110**, 2462 (2006).
29. P. Fenter *et al.*, *Surf. Sci.* **412–413**, 213 (1998).

30. We thank INFM's Parallel Computing Initiative and the San Diego Supercomputing Center (SDSC) for CPU time, and M. Tatineni at SDSC for help with getting early access to new TeraGrid resources. Supported by Ministero dell'Università e della Ricerca PRIN 2006020543 and FIRB NOMADE and by NSF grant CHE-0626354.

Supporting Online Material

www.sciencemag.org/cgi/content/full/321/5891/943/DC1
Materials and Methods
References

1 April 2008; accepted 8 July 2008
10.1126/science.1158532

Smoke Invigoration Versus Inhibition of Clouds over the Amazon

Ilan Koren,[1] J. Vanderlei Martins,[2,3] Lorraine A. Remer,[3] Hila Afargan[1]

The effect of anthropogenic aerosols on clouds is one of the most important and least understood aspects of human-induced climate change. Small changes in the amount of cloud coverage can produce a climate forcing equivalent in magnitude and opposite in sign to that caused by anthropogenic greenhouse gases, and changes in cloud height can shift the effect of clouds from cooling to warming. Focusing on the Amazon, we show a smooth transition between two opposing effects of aerosols on clouds: the microphysical and the radiative. We show how a feedback between the optical properties of aerosols and the cloud fraction can modify the aerosol forcing, changing the total radiative energy and redistributing it over the atmospheric column.

The effect of aerosols on clouds and precipitation contributes the largest uncertainty to the estimation of the anthropogenic contribution to climate change. There are two main pathways by which aerosols can change cloud properties: microphysical and radiative processes (*1*, *2*). Changes in aerosol particle concentration produce changes in the size distribution of the cloud droplets (because aerosols function as cloud condensation nuclei) and therefore affect condensation and evaporation rates, latent heat release, collision coalescence efficiency, and related cloud properties such as reflectance, lifetime, phase, size, and precipitation (*3*–*5*).

Additionally, the absorption of aerosols can change the atmospheric stability profile by heating the aerosol layer and cooling the layers below. This may stabilize shallow layers and reduce their relative humidity, suppress moisture and heat fluxes from the surface, and suppress shallow cloud formation inside or below the aerosol layer (*6*, *7*), while destabilizing the profile above the aerosol layer.

The microphysical and the radiative pathways of interaction initiate many feedbacks that add complexity to the system and have different sensitivities to the aerosol loading. Clouds are sensitive to the initial concentration and size distribution of the potential cloud condensation nuclei (CCN). For a given aerosol type (size distribution and chemistry), clouds have a logarithmic sensitivity to the amount of potential CCN (*8*–*10*). Small changes in the aerosol loading in clean environments (a low CCN concentration of ~100 CCN/cm^3) will potentially change the cloud properties (fraction, optical depth, and droplet size distribution) much more than similar changes when the cloud is polluted (a CCN concentration of ~1000 CCN/cm^3) and the effect approaches saturation. In contrast, the absorption of electromagnetic energy (mostly in the visible and near-infrared range) by aerosols has a completely different sensitivity to aerosol loading. The overall absorption of energy increases steadily with the aerosol loading, and the increasing rate depends on the diurnal cycle of solar flux (geometry), aerosol optical properties, surface albedo, and the depths of the aerosol layer (*11*).

In this paper, we develop a theoretical basis that ties together the two pathways and explores the relationships of cloud amount and vertical development to aerosol optical thickness (τ), a proxy for CCN and for the potential to absorb solar energy. We find a smooth transition between these two pathways in an observational data set obtained over the Amazon.

The (aerosol) absorption (cloud) fraction feedback (AFF) can be described as follows: Aerosol absorption of solar radiation heats the aerosol layer and cools the surface, stabilizing the temperature profile and reducing relative humidity and surface moisture fluxes (evapotranspiration). This effect reduces cloudiness. Reduced cloud coverage exposes greater areas of the aerosol layer to direct fluxes from the Sun and therefore produces more intense heating of the aerosol layer, further reducing cloudiness. This positive feedback will be balanced once the extra heating of the surface raises the surface temperature sufficiently to destabilize the profile again and to transfer the humidity concentrated

---

[1] Department of Environmental Sciences, Weizmann Institute, Rehovot 76100, Israel. [2] Department of Physics and Joint Center for Earth Systems Technology, University of Maryland Baltimore County, Baltimore, MD 21250, USA. [3] Laboratory for Atmospheres, NASA Goddard Space Flight Center, Greenbelt, MD 20771, USA.

near the surface to higher levels in the atmosphere, therefore promoting cloud formation.

If we assume that the surface temperature response is relatively slow compared to changes in the solar flux, a basic description of this system can be expressed analytically, assuming that the cloud fraction C_f depends linearly (*6*, *12*) on changes in the aerosol layer temperature T

$$C_f = C_{f0} - a(T - T_0) \qquad (1)$$

where C_{f0} and T_0 are the cloud fraction and the temperature for the pristine atmosphere and a (1/°C) is the proportionality constant that determines the sensitivity of cloud fraction to temperature changes.

For a given surface albedo and type of aerosol, the rate of change in the temperature of the aerosol layer dT/dt is proportional to the aerosol optical depth τ (*11*) and to the fraction of cloud-free sky ($1 - C_f$) allowing direct interaction of the solar flux with aerosols

$$dT/dt = \tau Q(1 - C_f) \qquad (2)$$

where Q (°C/s) is a proportionality constant that depends on the aerosol optical properties and heat capacity of the layer.

Solving this system for T and C_f

$$T = T_0 - \frac{(1 - C_{f0})}{a}[1 - \exp(a\tau Qt)] \qquad (3)$$

and

$$C_f = 1 - (1 - C_{f0})\exp(a\tau Qt) \qquad (4)$$

yields an exponential dependence of the temperature T and the cloud fraction C_f in time. The cloud fraction depends on two components: the exponent that holds all the physical parameters (heat capacity, amount of aerosol absorption, and response of the clouds) multiplied by the initial fraction of clear sky ($1 - C_{f0}$). This shows that the radiative response of the system to a given environmental condition (a, τ, Q) in a given time depends on the initial cloud fraction C_{f0}. Smaller C_{f0} will yield a faster reduction in cloud fraction.

The logarithmic response of the cloud fraction to microphysical effects, shown in several observation and modeling studies (*8*–*10*, *13*–*16*), is simulated empirically by

$$C_{fm} = C_{fs}\left(1 - \exp\left(-\frac{1}{b}\tau\right)\right) \qquad (5)$$

where C_{fm} is the cloud fraction under the influence of the microphysical effect, C_{fs} is the saturation cloud fraction, and b is a parameter determining how fast the logarithmic effect saturates (*11*). The cloud fraction, represented empirically by Eq. 5, is the end result of all the aerosol effects and feedbacks on cloud microphysics.

Assuming the independence of the microphysical and radiative processes, and because the time response of the microphysical is much shorter than that of the radiative effects, the microphysical cloud fraction C_{fm} can approximate the initial cloud fraction C_{f0} of the radiative effect. Therefore, a superposition of the two effects yields

$$C_{ft} = 1 - (1 - C_{fm})\exp(a\tau Qt) \qquad (6)$$

The total cloud fraction C_{ft} (Eq. 6) can be approximated well by a superposition of two separate curves. One represents the microphysical effect (Eq. 5) and one the radiative effect (Eq. 4). The saturation cloud fraction from the microphysical process serves as the initial cloud fraction for the absorption processes ($C_0 = C_{fs}$). Figure 1 shows a conceptual scale analysis of the separated processes and the superposition of the two effects, as given by Eqs. 4 to 6. The equation constants were estimated by running a radiative transfer model with typical Amazonian profiles and smoke (*11*) and from previous studies (*6*, *10*, *15*, *16*). The absorption effect that appears almost linear in the plots is actually (slowly) exponentially decreasing, and the slopes that represent the reduction rate in cloud fraction due to absorption change as a function of the cloud fraction. For the same absorption properties and $\tau = 2$, the maximum reduction in cloud fraction is 3% for $C_{f0} = 0.9$, 18% for $C_{f0} = 0.5$, and clouds have completely disappeared for $C_{f0} = 0.2$. With a smaller initial cloud fraction, the absorption effect begins to dominate at lower values of τ. The τ of maximum cloud fraction is 0.55 for $C_{f0} = 0.9$, 0.40 for $C_{f0} = 0.5$, and 0.3 for $C_{f0} = 0.2$.

To observe the effect of aerosol on cloud cover, we used Moderate Resolution Imaging Spectroradiometer retrievals of cloud and aerosol properties (*11*, *17*–*19*) over the Amazon in the dry season, when the region experiences consistent meteorological conditions (*11*, *20*). The cloud data, cloud fraction C_{ft}, and cloud-top pressure P (a measure proportional to the cloud vertical development) were sorted as a function of τ and averaged for each 50 samples, producing one τ, C_{ft}, and P value on the scatter plot (Fig. 2, upper row). Pixels with $\tau > 0.8$ were removed to avoid a higher probability for misclassification of clouds and aerosols in high-τ regimes (*21*). Next, to show how the cloud fraction feedback changes the absorption rate, the same analysis was done on subsets of the data with cloud fraction <0.5 (Fig. 2, lower row).

Although the data for the pressure dependence on τ are scattered, the stronger absorption effect is noticeable for the smaller cloud fraction set with an absolute change of cloud fraction ΔC_{ft} of ~10% from the peak (maximum cloud fraction) to τ maximum, for the whole data set and ~15% for the lower cloud fraction. The relative change in cloud fraction defined as $\Delta C_{ft}/\max(C_{ft})$ is much larger for the lower fraction set (~0.47) as compared to the whole data set (~0.18). The τ at the curve maximum is shifted from ~0.3 for the whole set to ~0.2 for the lower cloud fraction set, as in the theoretical results (Fig. 1). Repetition of the same analysis on 2006 and 2007 data yielded almost identical results between 2007 and 2005. The 2006 results showed the same functional relationships but ~50% of the radiative effect at higher τ, which we attribute to very different burning and smoke conditions that year (*22*).

Cloud fraction correlates well with cloud-top height (vertical development) (Fig. 3, upper right). Therefore, by filtering out the pixels with the large C_{ft}, the data may be biased to lower,

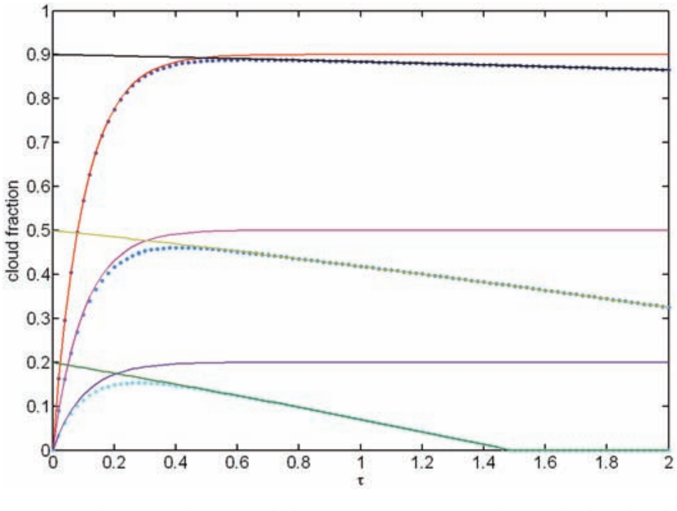

Fig. 1. Conceptual model of microphysics and absorption effects on cloud fraction for three saturation/initial cloud fractions C_{f0}. The absorption effect is simulated (Eq. 4) with characteristic time response t = 3 hours, a modest cloud fraction response to change in temperature $a = 0.05°C^{-1}$, and an atmospheric heating constant Q = 1°C per 3 hours per $\tau = 1.0$. We ran this simulation for three cases of saturation cloud fraction C_{f0}. The overall effect is a superposition of the microphysics and absorption processes and was calculated with Eq. 6. Case 1 (red, blue, and black lines): $C_{f0} = 0.9$. The red line shows the cloud-fraction dependence on the microphysics, the black line shows the reduction due to absorption, and the dotted blue line is the overall effect. Case 2 (magenta, turquoise, and gold): $C_{f0} = 0.5$. The magenta line shows the cloud-fraction dependence on the microphysics, the gold line shows the reduction due to absorption, and the dotted turquoise line is the overall effect. Case 3 (purple, green, and light blue): $C_{f0} = 0.2$. The purple line shows the cloud-fraction dependence on the microphysics, the green line shows the reduction due to absorption, and the dotted light blue line is the overall effect.

less-developed clouds. To see the combined effects of aerosols on clouds as a function of the cloud-top height, we did the following: First the data were sorted from clean to polluted by τ and divided into five equal sample subsets, from clean (blue) to most polluted (purple). Then each subset variable (τ and C_{ft}) was sorted by *P* and plotted, in Fig. 3, after application of a running average window of 100 samples (*10*). This processing was performed twice, once for the whole data set and once for the data filtered by $C_{ft} < 0.5$.

The τ distribution versus *P* for the five groups is shown on the left side of Fig. 3. The polluted clouds reach higher levels of the atmosphere (*10*, *23*). We see on the C_{ft} distribution versus *P* for the whole data set (Fig. 3, upper right) that the boomerang shape of Fig. 2 (upper right) is apparent at most of the pressure levels, with a minimum C_{ft} for the clean case, a maximum for the medium pollution cases, and a moderate decrease in the C_{ft} for the most polluted (purple) set. For the shallowest clouds ($P > 850$ mb), the lowest C_{ft} occurs in the most polluted case.

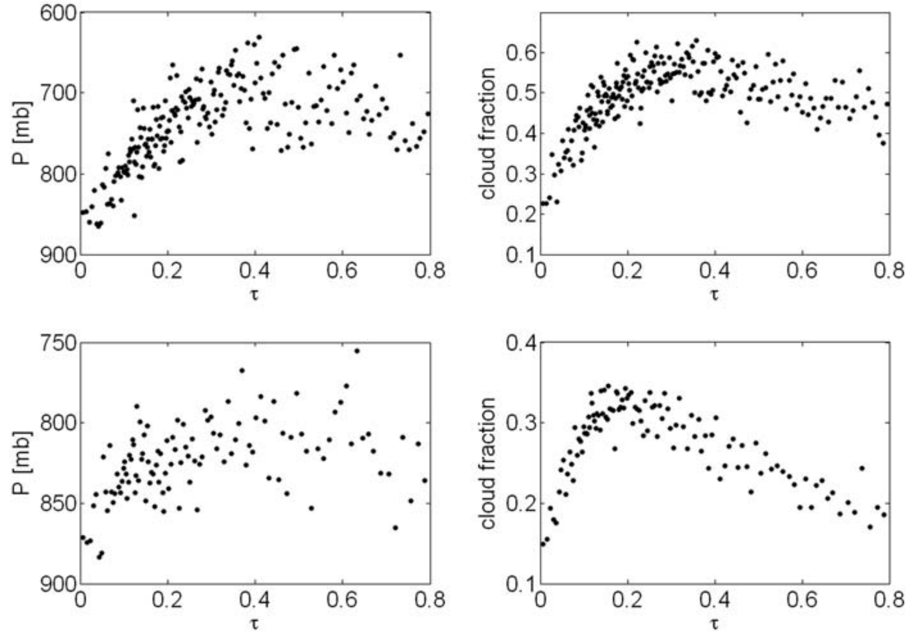

Fig. 2. Relationships between cloud properties and aerosol loading (estimated by τ). (**Left panels**) *P* versus τ. Lower *P* may indicate taller convective clouds that reach to higher levels of the atmosphere. (**Right panels**) Cloud fraction versus τ. The upper row shows all data and the lower row shows data restricted to a cloud fraction <0.5.

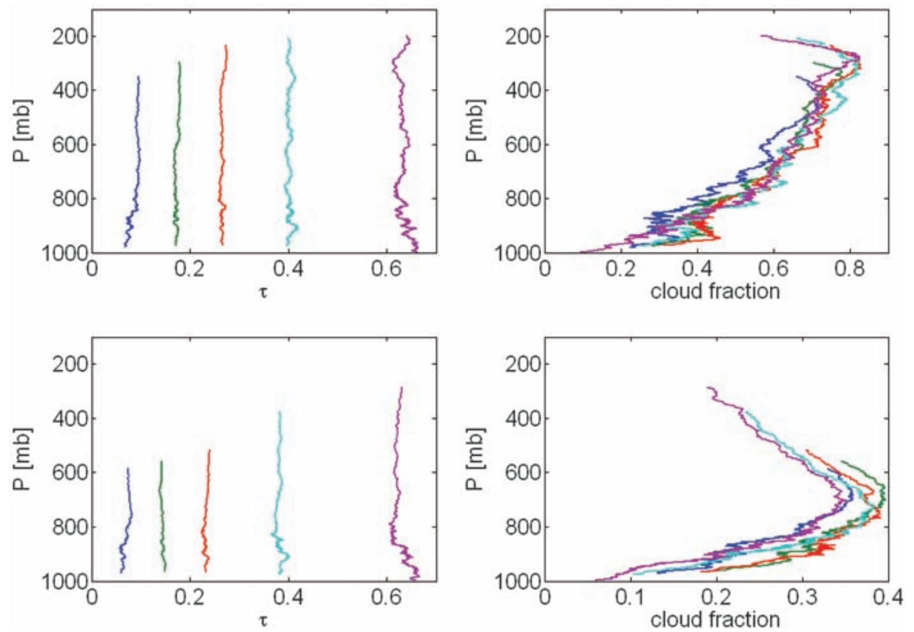

Fig. 3. Cloud fraction and τ divided into five subsets by τ, from the cleanest (blue) to the most polluted (purple) and plotted as a function of *P*. Results for the whole data set are plotted in the upper row; those for the subset of $C_{ft} < 0.5$ are plotted in the lower row. (**Left**) The average aerosol optical depth of the five subsets versus the pressure. (**Right**) Cloud fraction for the five τ subsets versus *P*. The cloud fraction scale is stretched for the filtered data (lower right).

The AFF becomes apparent when results from the whole data set are compared to the subset of $C_{ft} < 0.5$. By filtering out the data with large cloud fraction, we lose the higher clouds (the clean and medium cloud sets do not reach the same low pressure levels as before). A maximum in cloud fraction occurs in the middle atmosphere (700 mb), with a reduction in C_{ft} above it. The figure shows that at almost every level of the atmosphere, the most polluted set has the lowest cloud fraction. This corresponds to the deepening bend of the boomerang shape in Fig. 2 when cloud fraction is restricted by half. Additional analysis is shown in (*11*).

The theoretical construction predicts a smooth transition from a logarithmic microphysical effect dominating the trends in the lower τ values to the absorption effect that takes over as τ increases, creating a characteristic boomerang shape between cloud fraction and aerosol optical thickness. The theory predicts that the final cloud fraction is tied to the initial cloud fraction through the absorption effect of the aerosols (the AFF). Analysis of cloud data over the Amazon during the dry season of 2005 identified the same boomerang-shaped relationship between cloud fraction and aerosol optical thickness predicted by the analytical theory. In particular, we show that when the cloud fraction is restricted to less than 0.5, the absorption effect is stronger because of the larger interface between the direct solar radiation and the absorbing aerosols, as suggested by the AFF. The results are similar for higher clouds that are most likely above the smoke layer as well as clouds within the smoke layer, suggesting that over the Amazon, stabilizing the lower atmosphere and suppressing fluxes from the surface dominate the processes and can inhibit high and deep convective clouds even though the upper atmosphere can be less stable because of the smoke heating below.

The boomerang shape of C_{ft} (or *P*), increasing with τ until reaching a maximum and then decreasing as τ increases, makes the explanation of a superposition of the two effects—the internal (microphysical) and external (absorption)—robust. Other possible explanations such as meteorology driving both aerosol and clouds, artifacts of cloud and aerosol retrievals, or the existence of a smooth transition zone from clouds to aerosols (*24*, *25*) are not likely to produce such complicated relationships. In particular, a decrease in cloud fraction as τ increases cannot be explained by any identified retrieval artifacts or a continuum between aerosols and clouds. Furthermore, to reduce the likelihood of retrieval artifacts, the data were restricted to τ < 0.8 to reduce aerosol misclassification as cloud.

The findings presented here have important implications for estimates of aerosol effects on climate forcing. Aerosols can either invigorate clouds, increasing cloud fraction and height (a result of the microphysical effects), or inhibit clouds, decreasing cloud fraction and height (a result of aerosol absorption). These two processes are superimposed, and affect clouds of varying vertical development differently. Small shallow clouds will be mostly inhibited throughout the range of τ, leading to net positive climate forcing (warming), whereas medium- and high-level clouds will be strongly invigorated in the low-τ range, leading to negative climate forcing (cooling) and the inhibition of higher aerosol loading, which again leads to warming.

Initial cloud fraction plays a critically important role in determining the balance between the two effects. Cloud fields with large cloud coverage will be affected mostly by microphysics (invigoration), whereas fields with low fraction will be inhibited strongly by aerosol absorption. This can further polarize the atmospheric regimes in such a way that the overcast mode will last longer with thicker clouds, whereas scattered cloud fields will be suppressed, resulting in smaller coverage of thinner clouds. Such redistribution of energy not only changes the climate radiative energy balance but also can change local and regional dynamics and precipitation patterns.

These results should help provide a better understanding of the processes involved in making estimates of climate forcing through cloud/aerosol interaction. Furthermore, these results will be useful in their current form for incorporation in or testing of cloud-resolving or climate models.

References and Notes

1. Y. J. Kaufman, I. Koren, *Science* **313**, 655 (2006).
2. H.-F. Graf, *Science* **203**, 1309 (2004).
3. S. Twomey, *J. Atmos. Sci.* **34**, 1149 (1977).
4. H. Jiang, G. Feingold, *J. Geophys. Res.* **111**, D01202 (2006).
5. D. Rosenfeld, *Science* **287**, 1793 (2000).
6. I. Koren, Y. J. Kaufman, L. A. Remer, J. V. Martins, *Science* **303**, 1342 (2004).
7. G. Feingold, H. Jiang, J. Y. Harrington, *Geophys. Res. Lett.* **32**, L02804 (2005).
8. G. Feingold, L. A. Remer, J. Ramaprasad, Y. J. Kaufman, *J. Geophys. Res.* **106**, 22907 (2001).
9. Y. J. Kaufman, I. Koren, L. A. Remer, D. Rosenfeld, Y. Rudich, *Proc. Natl. Acad. Sci. U.S.A.* **102**, 11207 (2005).
10. I. Koren, Y. J. Kaufman, L. A. Remer, D. Rosenfeld, Y. Rudich, *Geophys. Res. Lett.* **32**, 10.1029/2005GL023187 (2005).
11. See supporting data on *Science* Online.
12. A. S. Ackerman *et al.*, *Science* **288**, 1042 (2000).
13. Y. J. Kaufman, T. Nakajima, *J. Appl. Meteorol.* **32**, 729 (1993).
14. M. Wetzel, L. Stowe, *J. Geophys. Res.* **104**, 31287 (1999).
15. A. Khain, D. Rosenfeld, A. Pokrovsky, *Q. J. R. Meteorol. Soc.* **131**, 2639 (2005).
16. G. Myhre *et al.*, *Atmos. Chem. Phys.* **7**, 3081 (2007).
17. S. Platnick *et al.*, *IEEE Trans. Geosci. Remote Sens.* **41**, 459 (2003).
18. R. C. Levy, L. Remer, S. Mattoo, E. Vermote, Y. J. Kaufman, *J. Geophys. Res.* **112**, D13211 (2007).
19. M. D. King *et al.*, *IEEE Trans. Geosci. Rem. Sens.* **41**, 442 (2003).
20. C. A. Nobre, L. F. Mattos, C. P. Dereczynski, T. A. Tarasova, I. V. Trosnikov, *J. Geophys. Res.* **103**, 31809 (1998).
21. J. I. Brennan, Y. J. Kaufman, I. Koren, R.-R. Li, *IEEE Trans. Geosci. Remote Sens.* **43**, 911 (2005).
22. I. Koren, L. Remer, K. Longo, *Geophys. Res. Lett.* **34**, L20404 10.1029/2007GL031530 (2007).
23. M. O. Andreae *et al.*, *Science* **303**, 1337 (2004).
24. I. Koren, L. A. Remer, Y. J. Kaufman, Y. Rudich, J. V. Martins, *Geophys. Res. Lett.* **34**, L08805 (2007).
25. R. J. Charlson, A. S. Ackerman, F. A. Bender, T. L. Anderson, Z. Liu, *Tellus B Chem. Phys. Meterol.* **59**, 715 (2007).

26. This paper is dedicated to the memory of Yoram J. Kaufman, a dear friend and a brilliant scientist. This research was supported in part by the Israel Science Foundation (grant no. 1355/06), and NASA's Interdisciplinary Science Program under the direction of H. Maring. I.K. is the incumbent of the Benjamin H. Swig and Jack D. Weiler career development chair at the Weizmann Institute.

Supporting Online Material

www.sciencemag.org/cgi/content/full/321/5891/946/DC1
SOM Text
Figs. S1 to S5
References

16 April 2008; accepted 8 July 2008
10.1126/science.1159185

Ferruginous Conditions Dominated Later Neoproterozoic Deep-Water Chemistry

**Donald E. Canfield,[1]* Simon W. Poulton,[2] Andrew H. Knoll,[3] Guy M. Narbonne,[4]
Gerry Ross,[5] Tatiana Goldberg,[2] Harald Strauss[6]**

Earth's surface chemical environment has evolved from an early anoxic condition to the oxic state we have today. Transitional between an earlier Proterozoic world with widespread deep-water anoxia and a Phanerozoic world with large oxygen-utilizing animals, the Neoproterozoic Era [1000 to 542 million years ago (Ma)] plays a key role in this history. The details of Neoproterozoic Earth surface oxygenation, however, remain unclear. We report that through much of the later Neoproterozoic (<742 ± 6 Ma), anoxia remained widespread beneath the mixed layer of the oceans; deeper water masses were sometimes sulfidic but were mainly Fe^{2+}-enriched. These ferruginous conditions marked a return to ocean chemistry not seen for more than one billion years of Earth history.

Early in Earth history, the deep oceans contained dissolved ferrous Fe, as documented by the widespread deposition of banded Fe formations (*1*). This condition expressed low atmospheric oxygen and low seawater sulfate concentrations in combination (*2*). The former limited the transport of oxygen into the deep ocean, whereas the latter limited rates of sulfide production by sulfate-reducing prokaryotes; without the low sulfate, the oceans would have been sulfidic, something like the modern Black Sea. Indeed, current models suggest that sulfidic deep-ocean conditions did become widespread around 1840 million years ago (Ma) as a result of increasing sulfate concentrations, and that this condition may have persisted through much of the Mesoproterozoic Era [1.6 to 1.0 billion years ago (Ga)] [(*3*–*6*); however, see (*7*) for another view].

The emergence of diverse animals by the end of the Neoproterozoic Era indicates a probable change to more oxic ocean and atmospheric conditions (*8*), but the course of this change is unclear. For example, despite a long-term increase in seawater oxygenation, iron formations recurred in association with globally extensive Neoproterozoic glaciations (*9*). An important pillar of the Snowball Earth hypothesis that maintains the Earth was completely covered in ice during significant periods of the Neoproterozoic, these iron formations are thought to represent the accumulation of Fe^{2+} in an ice-capped anoxic ocean (*10*, *11*). Ferruginous deep-ocean waters were also associated with the later Gaskiers ice age (580 Ma) (*12*), but deep-water oxygenation followed deglaciation, at least on the Avalon Peninsula, Newfoundland. Was this deep-water oxygenation, however, local or global, and was it the first time that oxygen pervaded deep waters during the Neoproterozoic era? Also, what is the relationship between short, ice age–associated intervals of iron deposition and the broader evolution of Neoproterozoic atmospheric and oceanic chemistry? Finally, and more broadly, how does Neoproterozoic ocean chemistry link the probable widespread occurrence of Mesoproterozoic sulfidic marine conditions with the predominantly oxic conditions of the Phanerozoic Eon (the past 542 Ma)? These outstanding issues invite further exploration of Neoproterozoic ocean chemistry.

We evaluated the redox chemistry of the marine water column by considering the speciation of Fe in well-preserved Neoproterozoic sedimentary rocks. With a calibrated Fe extraction proce-

---

[1] Nordic Center for Earth Evolution and Institute of Biology, Campusvej 55, University of Southern Denmark, 5230 Odense, Denmark. [2] School of Civil Engineering and Geosciences, Newcastle University, Drummond Building, Newcastle upon Tyne NE1 7RU, UK. [3] Botanical Museum, Harvard University, Cambridge, MA 02138, USA. [4] Department of Geological Sciences and Geological Engineering, Queen's University, Kingston, Ontario K7L 3N6, Canada. [5] Kupa'a Farm, Post Office Box 458, Kula, HI 96790, USA. [6] Geologisch-Paläontologisches Institute der Universität Münster, Correnstrasse 24, Münster 48149, Germany.

*To whom correspondence should be addressed. E-mail: dec@biology.sdu.dk